The International Journal of Advanced Manufacturing Technology (2019) 101:1007–1021
https://doi.org/10.1007/s00170-018-3005-7

ORIGINAL ARTICLE

# Surface microstructure of titanium alloy thin-walled parts at ultrasonic vibration-assisted milling

Jinglin Tong[1] · Guan Wei[1] · Li Zhao[1] · Xiaoliang Wang[1] · Junjin Ma[1]

Received: 15 May 2018 / Accepted: 6 November 2018 / Published online: 12 November 2018


## Abstract

Milling of the titanium alloy thin-walled workpiece is a critical challenging task and the machining vibration is a major effect on the accuracy of the final part due to difficult machining properties and low stiffness. The common milling (CM) is very hard for titanium alloy thin-walled parts to get high-quality machined surface microstructure, so finding an effective way of processing to obtain better surface microstructure is particularly important. In this article, the longitudinal-torsional composite ultrasonic vibration-assisted milling (LTCUVM) is proposed to overcome the problems of the common milling. The cutting method of the high-frequency vibration separation of a workpiece and the tool reduces an average cutting force. Thereby suppressing the tool relieving and further providing a good machined surface. In this study, firstly, the kinematic model of LTCUVM was established and the variations of the movement of the cutting edge flank with the spindle speed change were analyzed. Then the finite element model (FEM) of the two processing methods was developed and significant differences between the CM and LTCUVM in the micro-milling were revealed. Further, related experiments were designed and conducted. Finally, the experimental analysis showed that the LTCUVM effectively reduced an average cutting force, and further reduced surface roughness and height of chatter marks compared to the CM with the same processing parameters.

**Keywords** Ultrasonic vibration-assisted milling · Titanium alloy thin-walled parts · Cutting force · Surface microstructure · Flank milling

## 1 Introduction

Titanium alloy material is one of the key materials with a range of significant performance advantages, it is widely used in aerospace, petrochemical and medical equipment, and other fields, especially for a large number of applications in aerospace engine manufacturing [1]. However, currently, there are two difficulties to be solved for the processing of titanium alloy workpieces. Firstly, titanium alloy materials have poor thermal conductivity, thus the machining surface can easily form severe work hardening, resulting in poor cutting performance, and this is a typical difficult-to-machine material [2]. Secondly, the wall thickness design and development of parts tend to be thinner, the dimensional accuracy of the critical surface of the workpiece, a position-shape error, and surface quality must be best possible. However, in the machining of thin-walled parts, the thin sections are elastically deformed under the cutting forces. Therefore, it is quite difficult to maintain dimensional accuracy and provide the required surface finish. The processing methods of titanium alloy thin-walled parts are a bottleneck in modern industry and cause concerns [3]. Although EDM, electrochemical machining, and laser forming technology are also the hot-spot machining methods, the cutting technology is still the main manufacturing method for titanium alloy thin-walled parts [4]. Meshreki et al. developed a new research model for the dynamic analysis and deformation prediction of weakly rigid structures based on the Barry-Rich method [5]. Bolar et al. optimized the machining parameters in the process of end-milling titanium alloy thin-walled parts, found optimal processing parameters, and established the related prediction model [6]. Smith et al. proposed the distributed ring cutting method and the large cutting depth method to process weak rigid structural elements to control the processing deformation [7].

✉ Jinglin Tong
tongjinglin@hpu.edu.cn

Guan Wei
weiguan0615@qq.com

[1] School of mechanical and power engineering, Henan Polytechnic University, Jiaozuo City 45400, Henan province, China

The ultrasonic vibration-assisted cutting (UVAC) is a machining method that applies ultrasonic vibration to the tool (or workpiece) to achieve pulsed intermittent cutting based on the common cutting, then achieves permanent macroscopic cutting and tool-chip separation microscopically, thereby intermittent cutting effectively reduces the cutting temperature and improves cutting performance. Experimental studies also showed that UVAC achieved significant breakthroughs in the machining of titanium alloys [8, 9]. Sui et al. performed a feasibility study of the high-speed ultrasonic vibration-assisted cutting (HUVC) of titanium alloys and pointed out that HUVC provided lower cutting force, increased the tool life, reduced chip deformation, and increased the material removal rate [8]. Shamoto et al. believed that elliptical vibration cutting could differentiate the cutting trajectory and improve the machining accuracy [10]. Xiao et al. found that ultrasonic vibration cutting suppressed chatter of tools and improved machining quality [11]. Nath et al. indicated that surface roughness has a higher lift at lower cutting speeds by optimizing the UVAC process parameters and comparing with the common cutting (CC) [12]. Shen et al. used ultrasonic vibration-assisted micro-milling of titanium alloy materials to study the effects of cutting parameters on the roughness of the machined surface and obtained optimal processing conditions [13]. Muhammed compared a change in the cutting force between the ultrasonic vibratory cutting and ordinary cutting based on the 3D FEM, and believed that the reason for the reduced cutting force is an increase of the cutting speed and the reduction of the tool working contact due to vibratory cutting [14]. Patil modeled the ultrasonic vibration-rotation machining and showed that the surface roughness in vibration-assisted turning (UAT) is lower than in common turning (CT), and the surfaces in UAT have matte finish as against the glossy finish at CT with 2D finite element analysis, it was verified that the degree of thermal softening of the material and the reduction of the shear strength of the material during vibration machining exceeded those at ordinary cutting [15]. Moaz used the finite element method to predict the effect of the feed rate on surface roughness during the titanium alloy milling and found an evident link between the feed cutting force and surface roughness at different feed rates [16]. Thepsonthi [1] and Ducobo [17] predicted tool wear at titanium alloy processing by using the finite element method. Many scholars have proved advances and effectiveness of the finite element analysis method. At the same time, the finite element analysis can simplify an experiment, find optimal theoretical parameters, and guide an experiment. Especially in the multi-parametric tasks, it has important guidance and prediction in the coupling effect analysis of experimental results.

Many scholars significantly improved UVAC processing accuracy, processing efficiency, and surface microstructure of titanium alloy workpieces. However, the surface microstructure of titanium alloy thin-walled workpieces concerns to a few research fields, and there is no clear theoretical analysis and qualitative analysis of experimental data related to the influence of ultrasonic vibration on the surface microstructure of thin-walled parts. Moreover, when the thin-walled part is processed, a thin-walled element is elastically deformed by the cutting force and the tool relieving is initiated. Therefore, maintaining dimensional accuracy and imparting the desired surface finish is quite difficult.

In this paper, we present theoretical-simulation and experimental combined analysis of LTCUVM processing methods for titanium alloy thin-walled parts, and explore the influence of LTCUVM and CM on the cutter force and surface microstructure of titanium alloy thin-walled parts at different speeds.

## 2 Modeling of the tooltip trajectory in the LTCUVM

LTCUVM is a method that applies high-frequency periodic vibrations in both the circumferential and axial directions of the tool, and two-dimensional ultrasonic vibration-assisted processing is performed on the basis of the common milling. The schematic diagram of the ultrasonic vibration flank milling titanium alloy thin-walled system is shown in Fig. 1.

### 2.1 Principle of LTCUVM

In the stable cutting state, a tool performs regular rotation machining on one side of a workpiece. The cutting edge only has a feed speed in the *X*-direction, which is the feed direction. Therefore, the machining method is flank milling. The *Y*-direction is the radial depth, and the *Z*-direction is the

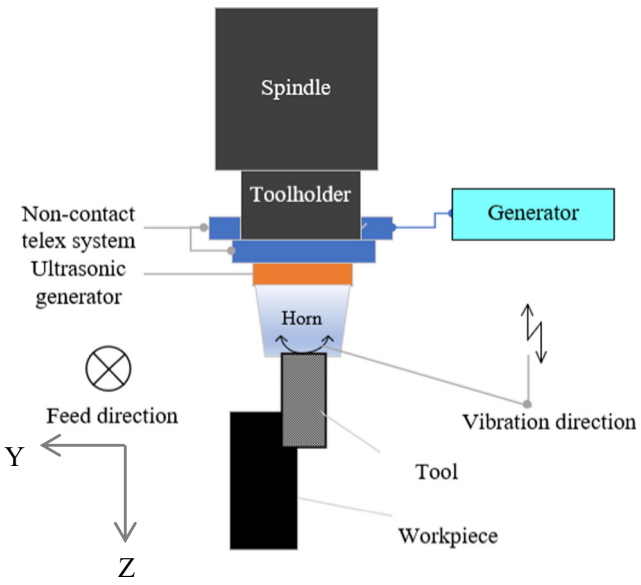


**Fig. 1** The ultrasonic vibration-assisted flank milling system

longitudinal depth. There are only longitudinal and torsional harmonic vibrations in *Y*- and *Z*-directions, as shown in Fig. 1.The cutting edge motion equation of LTCUVM is the following:

$$\begin{cases} x(t) = v_f \cdot t + r \cdot \sin(\phi) \\ y(t) = r \cdot \cos(\phi) \\ z(t) = L \cdot \sin(2\pi f t) \end{cases} \quad (1)$$

In Eq. (1), $v_f$ is the feed speed, mm/min, and can be expressed by the formula as follows:

$$v_f = f_z \cdot n \cdot z \quad (2)$$

where $f$ is the longitudinal and torsional ultrasonic vibration frequency, kHz; $r$ is the tool radius, mm; mm/s; $L$ is the amplitude of the longitudinal vibration in LTCUV, mm. $fz$ is the feed per tooth, mm/z. $z$ is the number of cutter teeth. $\phi$ is the actual corner of the tool, rad, which can be expressed by the formula as follows:

$$\phi = 2 \cdot \pi \cdot (n/60 \cdot t) + \theta \quad (3)$$

where $n$ is the spindle speed, r/min; $\theta$ is the angle of the torsional vibration in LTCUV, rad, which can be expressed by the formula as follows:

$$\theta = T \cdot \cos(2\pi f t + \varphi) \quad (4)$$

$T$ is the amplitude of the torsional vibration in LTCUV, rad; $\varphi$ is the phase difference between the longitudinal vibration and the torsional vibration, rad.

The joint point and separation point of the cutting edge and a workpiece are solved by the discretization of the cutting edge trajectory. The path of the cutting edge trajectory was discretized and the value of the spatial angle corresponding to each discrete point was calculated. Moreover, the separation point was determined by solving the corresponding spatial spiral angle $\beta$ of each point along the tool path, and then the spiral angle formed by the line connecting each point after the separation point was solved, whether the two spiral angles are equal to the tool helix angle $\beta$ to solve the separation point and joint point between the cutting edge and the workpiece. The comparison between the actual spatial angle of the discrete points in the cutting edge trajectory and the tool helix angle was basic for judging whether the cutting edge participates in the cutting to obtain the contact between the tool and the workpiece. The separation of the tool path is shown in Fig. 2.

The three-dimensional tool tip trajectory of LTCUVM is shown in Fig. 2. A1, A2, and A3 are the separation points between the tool and the workpiece. B1, B2, and B3 are the joints between the tool and the workpiece. The cutting edge is separated from the workpiece during the movement from A1 to B1, and contact with the workpiece is started from B1 until it is separated from the workpiece again by the movement to A2. The LTCUVM cutting process is thus formed and repeated. Among them, B1 to A2 segments, and B2 to A3 segments are the cutting edges involved in the cutting process, then A1 to B1 segments, A2 to B2 segments, and A3 to B3 segments are processes of the cutting edges separation from the workpiece. The percentage of the actual cutting time of the tool in a separation-joint cycle is called the duty cycle.

### 2.2 Duty cycle

The duty cycle is one of the most important parameters describing the LTCUVM process and its separation characteristic. The duty cycle varies substantially at spindle speed change. Taking the simulation parameters in Table 1 as the cutting conditions, the cutting edge trajectory at 1200 r/min, 1600 r/min, 2000 r/min, 2400 r/min, 2800 r/min, and 3200 r/min was studied (as shown in Fig. 3a–f).

From Fig. 3a–h, it can be clearly seen that point A was gradually combined with point B, which means that the real cutting time of the cutting edge at the ultrasonic vibration cycle increases, and the separation time decreases. From a to c, it can be seen that the cutting edge path rotates during the cutting process, but after the d (rotation speed 2400 r/min), the cutting edge no longer cuts rotary. The spindle speed exceeds the critical revolving speed of 2100 r/min. After this critical value, the tool does not rotate. When the rotation speed reaches 3200 r/min (Fig. 3f), the separation points A and the next joint points B basically coincide. So, when the spindle critical speed exceeded, the cutting edge no longer exhibits tool-chip separation during the cutting process. The critical speed of LTVUVM is 3208 r/min under these parameters.

The duty cycle calculation of LTCUVM is very complex, the corresponding fitting curve can be obtained by calculating the value of the duty cycle at different speeds. As shown in Fig. 4, as the spindle speed was increased, the duty cycle increased as well, meanwhile, the actual cutting time increased within a single ultrasonic vibration cycle. With the spindle speed increase, the milling cutter-workpiece separation time of the LTVUVM during the cutting will be reduced, even down to 0, thereby the cutting state of the LTVUVM changes.

This special vibration-separated tool path undoubtedly makes the flank milling of titanium alloy thin-walled parts more delicate ($n$ is within the critical value), which is directly reflected in the cutting force signal output. Variation in the cutting force changes the state of the cutter relieving during milling the rigid thin-walled parts.

## 3 FEM and results

The cutting force is a key factor affecting deformation of a workpiece, it affects the microstructure of the machined

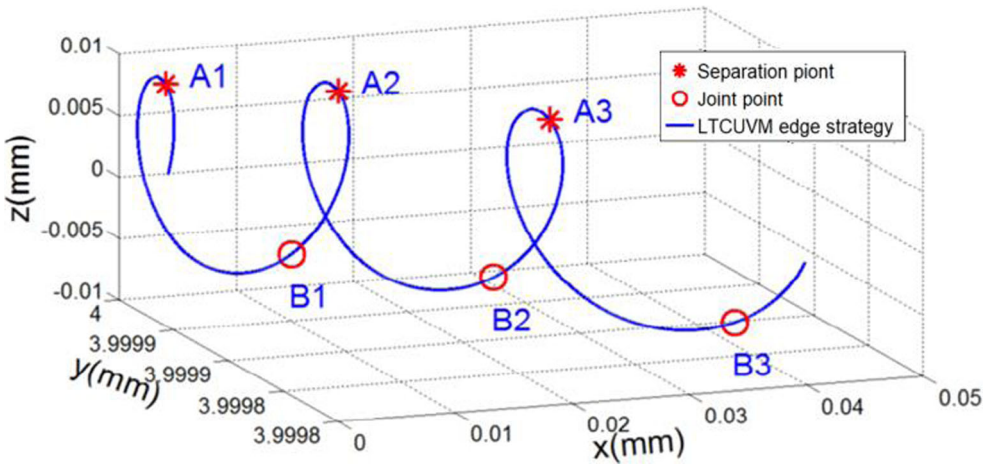


**Fig. 2** Tooltip trajectory of LTCUVM

surface. The cutting force during the flank milling titanium alloy thin-walled workpieces was estimated and analyzed by the finite element model (FEM) cutting simulation. The result explained the reasons for the variation in the force of experimental cutting force measurements at micro-level and further explained reasons for the appearance of the surface microstructure features in LTCUVM and CM. We developed a transient dynamical cutting model based on the universal finite element software ABAQUS. Then a finite element simulation was performed using the thermal-heat coupled iterative algorithm. Finally, the cutting force signal was simulated by the corresponding historical variables.

### 3.1 Cutting simulation model

The workpiece of TC4 titanium alloy was machined with YG8 milling tool for flank milling in FEM cutting simulation. The parameters of the tool, workpiece, and processing are shown in Fig. 5. The finite element cutting simulation algorithm was based on a force-thermal coupled iteration explicit algorithm. The *X*-direction (feed direction) speed and the circumferential speed around the *Y*-axis was given for the tool, while the harmonic vibration amplitude function in *Y*-direction was imparted to the tool and *X*-direction (equivalent for a tool torsional vibration) of the workpiece. The remaining loads at a speed direction were set to 0. Workpiece meshing was divided into sub-regions to reduce the calculation time. The grid unit used a simplified four-node temperature-displacement coupled reduction unit with good stability (as shown in Fig. 5; unit mm; $\alpha_p$ is the axial depth; $\alpha_e$ is the radial depth; $\beta$ is the tool helix angle).

**Table 1** Simulation parameters at a different spindle speed

| Simulation parameters | |
|---|---|
| Tool radius ($r$) | 4 mm |
| Helix angle ($\beta$) | 30° |
| Feed per tooth ($f_z$) | 0.09 mm/z |
| Frequency ($f$) | 35 kHz |
| Amplitude of the longitudinal wave($L$) | 8 μm |
| Amplitude of the torsional wave ($T$) | 0.001 rad |
| Phase difference ($\varphi$) | pi/2 |
| Spindle speed ($n$) | 800 r/min |
| Teeth ($z$) | 4 |

The flowchart of the dynamic thermal-coupled iterative algorithm is shown in Fig. 6. Firstly, the geometric model, boundary conditions, and initial conditions were defined. Secondly, four models: a material plastic constitutive model, damage model, friction model, and a heat transfer model were combined and dynamic algorithm of the FEM cutting model was displayed. Then the magnitude of plastic deformation at the cutting process, the corresponding stress-strain, flow stress, and strain energy were obtained, and it was further fed back to the tool, chip, workpiece, and environment in the form of heat. Moreover, it was iterated through the constitutive model after heat distribution and heat conduction steps. Finally, the cutting force was simulated taking into account the force-thermal coupled effect.

Used in this study Johnson-Cook plastic constitutive model [18] (Formula 4) added the heat softening temperature parameter in FEM. It better reflects the parameter of plastic constitutive changes with the temperature rise at material processing. J-C damage model was adopted for the fracture criterion of TC4 material [19, 20] (Formula 5). The friction model and the cutting heat conduction model refer to references [21, 22].

$$\overline{\sigma} = (A + B\varepsilon^n)\left[1 + C\ln\left(\frac{\dot{\varepsilon}}{\dot{\varepsilon}_0}\right)\right]\left[1-\left(\frac{T-T_{\text{room}}}{T_{\text{melt}}-T_{\text{room}}}\right)^m\right] \quad (5)$$

where $\sigma$ is the equivalent stress; $\varepsilon_0$ is the equivalent elastic strain; $\dot{\varepsilon}$ is the equivalent elastic strain rate; and $\dot{\varepsilon}_0$ is the reference equivalent elastic strain rate. $T$, $T_{\text{room}}$, and $T_{\text{melt}}$ are the deformation temperature, room temperature, and

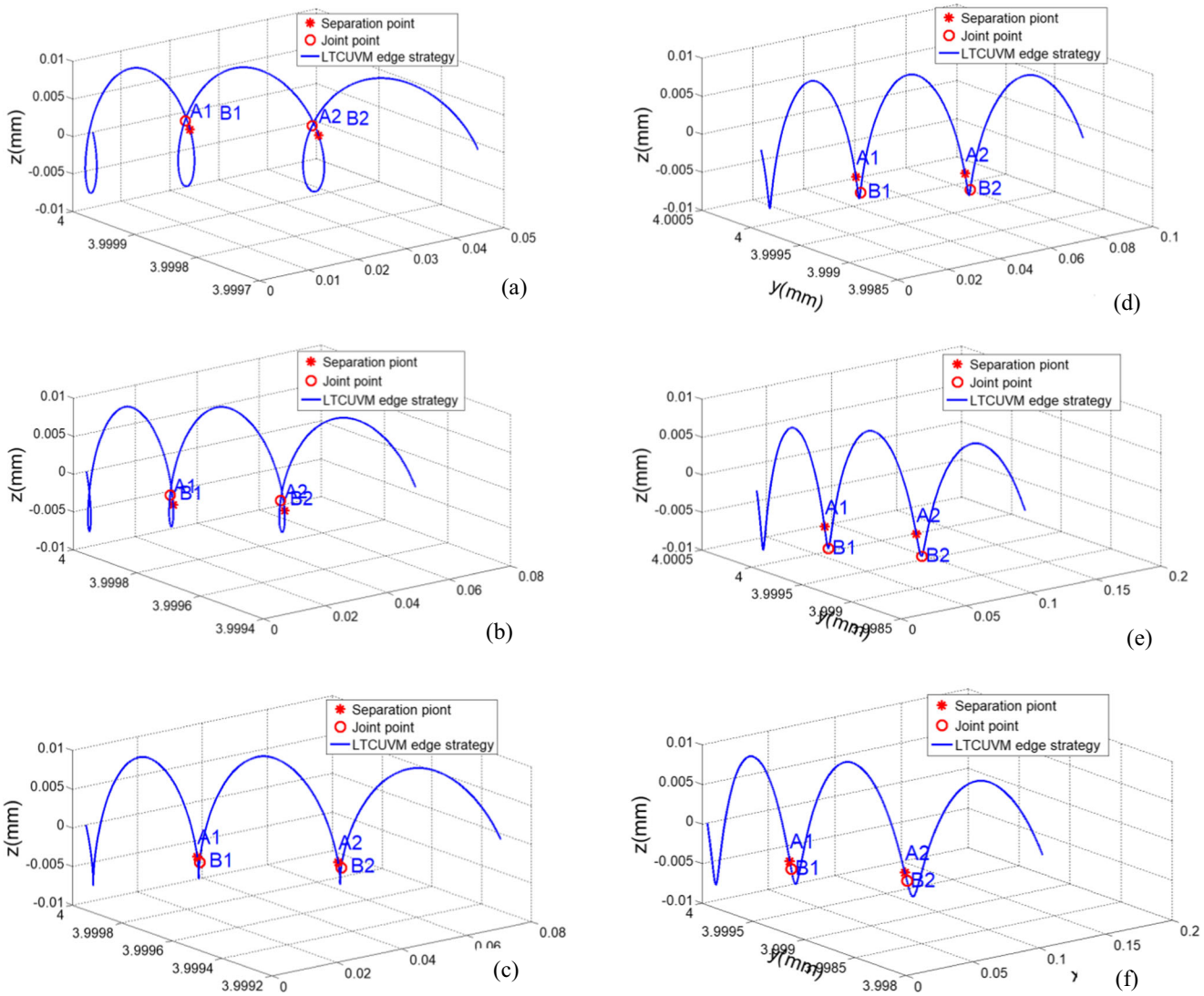


**Fig. 3** Effect of rotational speed on the tooltip trajectory at LTCUVM

melting temperature of a workpiece. $A$ is the yield stress, $B$ is the hardening modulus; $C$, $m$, and $n$ are the material's characteristic factors, thermal softening factor, and the work hardening index, which can be obtained through the compression rod tests [23]. The simulation parameters are shown in Table 2.

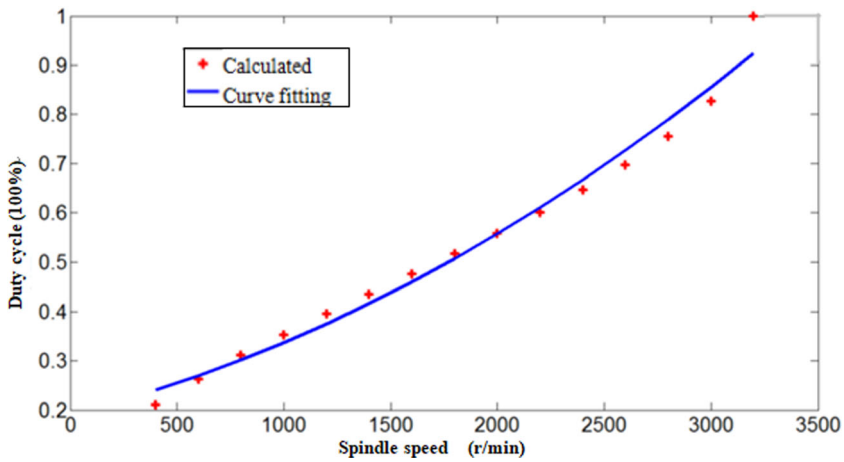


**Fig. 4** Duty cycle vs. spindle speed

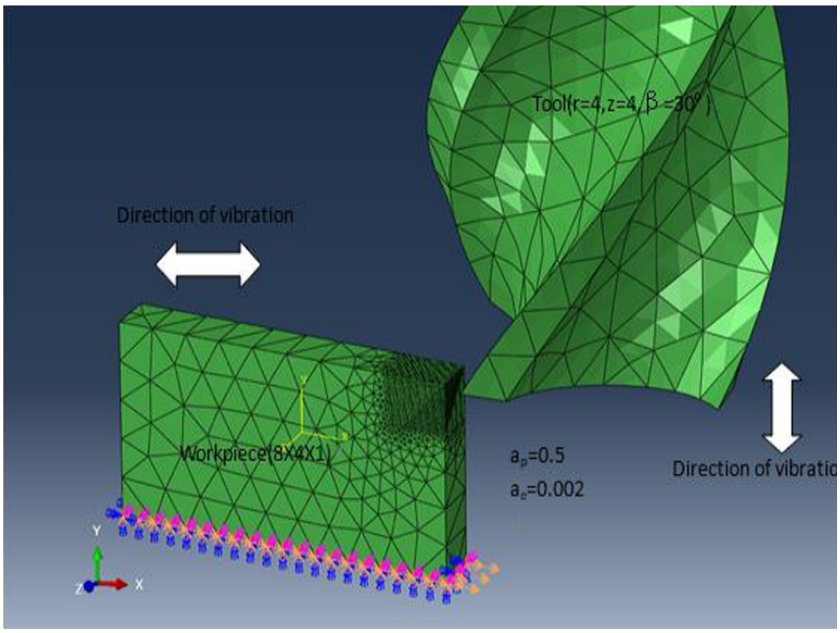


**Fig. 5** Finite element cutting simulation model

The fracture value of each unit in the J-C damage model can be determined by the following formula:

$$D = \sum \frac{\Delta \bar{\varepsilon}^{p}}{\bar{\varepsilon}^{pf}} \tag{6}$$

where $\Delta\bar{\varepsilon}^{p}$ is the equivalent plastic strain increment at the material integration point; $\bar{\varepsilon}^{pf}$ is the material failure strain. If $D > 1$, all materials at the integration point fail, the grid will be broken, the material unit fails, and chip separates from the workpiece. The failure strain can be obtained by the following formula:

$$\bar{\varepsilon}^{pf} = \left(D_1 + D_2 \exp D_3 \sigma^{*}\right)\left[1 + D4 \ln \frac{\dot{\bar{\varepsilon}}^{p}}{\dot{\bar{\varepsilon}}}\right]\left[1 - D_5\left(\frac{T - T_0}{T_{\text{melt}} - T_0}\right)^{m}\right] \tag{7}$$

where $D_1$, $D_2$, $D_3$, $D_4$, and $D_5$ are the damage parameters of the TC4 material, as shown in Table 3.

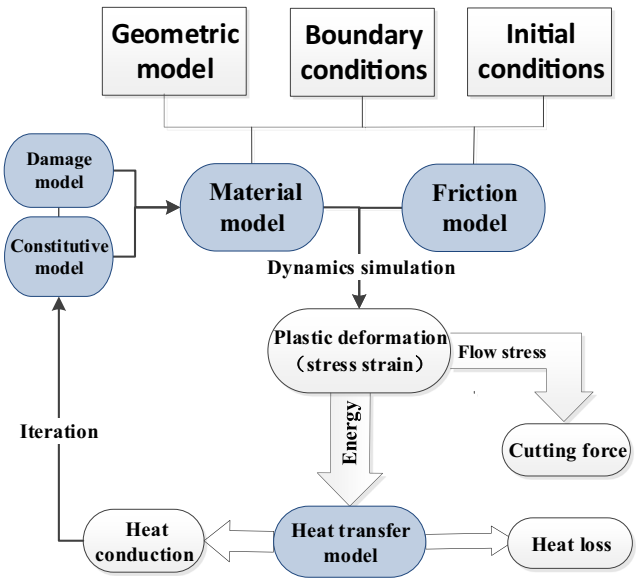


**Fig. 6** Flowchart of the dynamic thermal-coupled iterative algorithm

## 3.2 Analysis of simulation results

The comparison of the cutting force sign in LCTVUM and CM are shown in Fig. 7a, b. In the case of LCTVUM, the radial force $F_r$ and feed force $F_f$ show a peak in single vibration cutting cycle, and the cutting force decreased up to zero when the tool-workpiece was separated, while the cutting force $F_r$ and $F_f$ underwent small range fluctuations within a single cut without drops to zero in CM. This results provide an explanation for the smaller chatter marks appeared on the surface of the workpiece because the local peaks of the instantaneous cutting force exceed the force in CM under the same working condition.

These were the FEM cutting force simulation results of the single-tooth milling thin-walled parts in a short time interval. In order to compare simulation results with experiments, the accuracy of FEM was verified, and the difference between

**Table 2** Johnson-Cook plastic constitutive parameters of TC4

| $A$ (Mpa) | $B$ (Mpa) | $n$ | $C$ | $m$ | $T_{\text{melt}}$ (°C) |
|---|---|---|---|---|---|
| 876 | 793 | 0.01 | 0.386 | 0.71 | 1560 |

**Table 3** J-C damage model parameters

| $D_1$ | $D_2$ | $D_3$ | $D_4$ | $D_5$ |
|---|---|---|---|---|
| − 0.09 | 0.25 | − 0.5 | 0.0014 | 3.87 |

LCTUVM and CM in $F_r$ and $F_f$ was further studied, the cutting force signal was processed to obtain the average milling force during the single-tooth milling. The average radial force $\overline{F}_r$ and average feed force $\overline{F}_f$ are shown in Fig. 7c, d ($n$ = 1.2, 1.6, 2.0, 2.4, 2.8, and 3.2 (1000 r/min)). $\overline{F}_r$ and $\overline{F}_f$ in LTCUVM have been significantly reduced compared to the milling force in CM. The data analysis showed that the average radial cutting force was reduced from 17.4 to 31.3%, in Fig. 7c, and the average feed cutting force was reduced from 25.4 to 38.7% in Fig. 7d.

From the results of the cutting simulation FEM analysis, the reduction in the cutting force in LTCUVM due to the high-frequency separation of the workpiece and tool, so that the average cutting force is less than the cutting force in CM.

## 4 Experimental and measurement procedure

The primary objective of the present experimental studies was to analyze cutting forces and the effect of LTCUVM and CM on the surface microstructure of titanium alloy thin-walled parts at different rotation speeds. Two sets of comparative tests were designed and carried out, then the obtained surface microstructure was compared and analyzed using the relevant testing equipment.

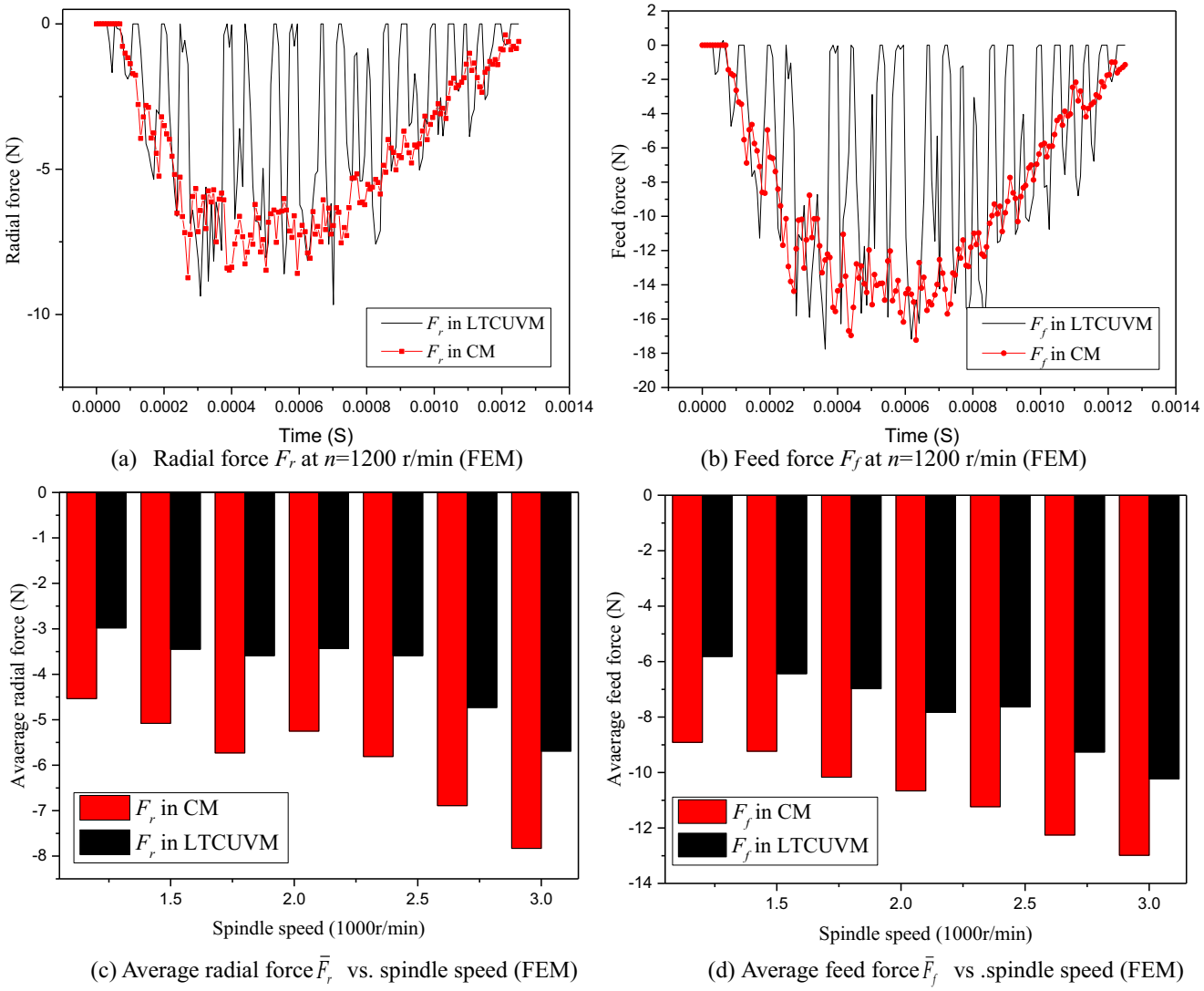


(a) Radial force $F_r$ at $n$=1200 r/min (FEM)

(b) Feed force $F_f$ at $n$=1200 r/min (FEM)

(c) Average radial force $\overline{F}_r$ vs. spindle speed (FEM)

(d) Average feed force $\overline{F}_f$ vs .spindle speed (FEM)

**Fig. 7** Comparison of the finite element cutting simulation results. **a** Radial force $F_r$ at $n$ = 1200 r/min (FEM). **b** Feed force $F_f$ at $n$ = 1200 r/min (FEM). **c** Average radial force $\overline{F}_r$ vs. spindle speed (FEM). **d** Average feed force $\overline{F}_f$ vs spindle speed (FEM)

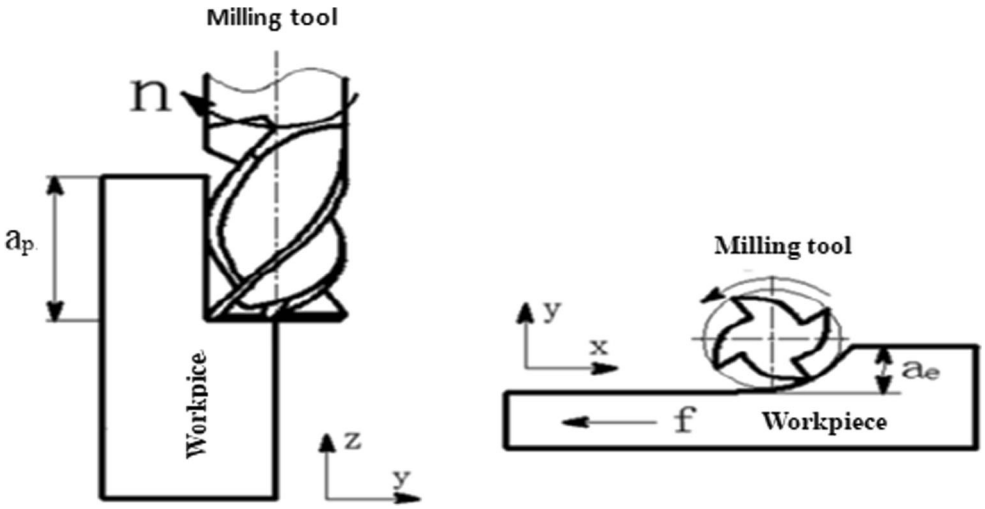


**Fig. 8** Schematic diagram of flank milling

## 4.1 Experimental procedure and parameters

As shown in Fig. 8, the workpiece of TC4 titanium alloy was machined with the YG8 tool in flank milling. The workpiece and tool-related parameters are shown in Table 4. Experimental equipment: a three-axis vertical machining center (MC-850); dynamometer (Kistler, sampling frequency: 30 kHz); and ultrasonic parameters: longitudinal amplitude $L = 6$ μm, torsional amplitude $T = 5$ μm, and tested ultrasonic resonance frequency 34.14 kHz. The experimental procedure is shown in Fig. 9. In order to study the changing trend of the surface appearance of the two flank milling operations with the change of the spindle speed, a single factor experiment was designed. The relevant processing parameters are shown in Table 5.

## 4.2 Experimental results and analysis

### 4.2.1 Analysis and comparison of cutting forces

The original partial cutting force signals in LTCUVM and CM are shown for comparison in Fig. 10; the signals of the radial feed forces were collected during rotation of the four-tooth milling cutter. There are two peaks and troughs in each graph representing the peak of the tool in both directions during

**Table 4** Characteristics of the workpiece and tool

| Workpiece | | Milling tool | |
|---|---|---|---|
| Material | TC4 | Material | Carbide |
| Elastic modulus [GPa] | 113.8 | Teeth | 4 |
| Density [kg/m3] | 4430 | Tool radius (mm) | 4 |
| Tensile strength [MPa] | 950 | Cutting edge length (mm) | 24 |
| Thermal conductivity [w/m•°C] | 7.3 | Tool length (mm) | 60 |
| Specific heat [J/(kg°C)] | 526 | Helix angle (°) | 30 |
| Size (mm) | 40 × 20 × 1 | | |

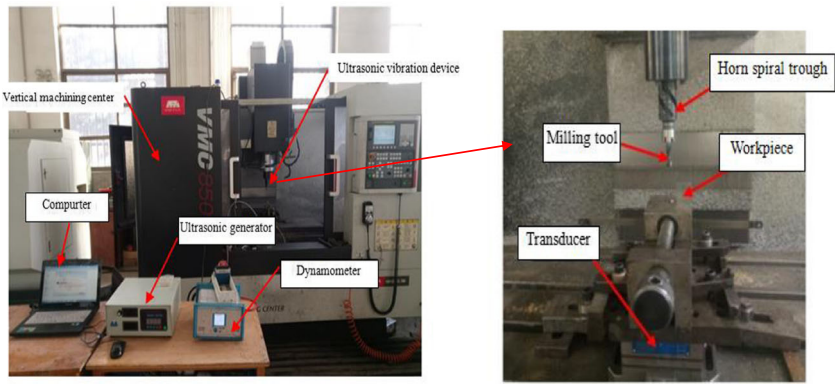


**Fig. 9** The experimental system of LTCUVM

**Table 5** Experimental parameters

| No. | Feed per tooth, $f_z$ (z/mm) | Spindle speed, $n$ (r/min) | Radial cutting depth, $a_e$ (mm) | Axial cutting depth, $a_p$ (mm) |
|---|---|---|---|---|
| 1 | 0.01 | 1000 | 0.05 | 5 |
| 2 | 0.01 | 1200 | 0.05 | 5 |
| 3 | 0.01 | 1400 | 0.05 | 5 |
| 4 | 0.01 | 1600 | 0.05 | 5 |
| 5 | 0.01 | 1800 | 0.05 | 5 |
| 6 | 0.01 | 2000 | 0.05 | 5 |
| 7 | 0.01 | 2200 | 0.05 | 5 |
| 8 | 0.01 | 2400 | 0.05 | 5 |
| 9 | 0.01 | 2600 | 0.05 | 5 |
| 10 | 0.01 | 2800 | 0.05 | 5 |
| 11 | 0.01 | 3000 | 0.05 | 5 |
| 12 | 0.01 | 3200 | 0.05 | 5 |

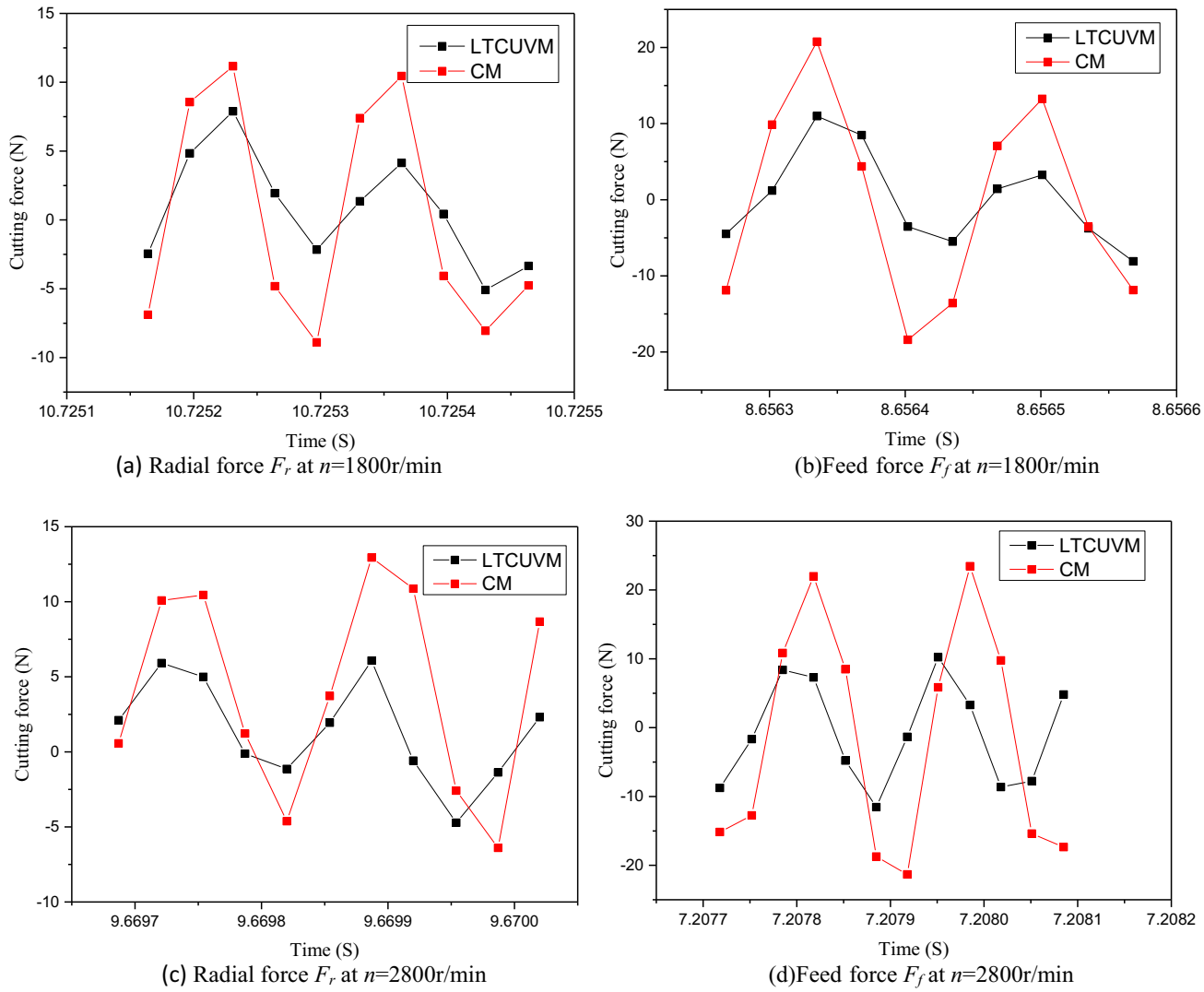


**Fig. 10** Comparison of the partial original cutting force signal between LTCUVM and CM ($n$ = 1800, 2800 r/min). **a** Radial force $F_r$ at $n$ = 1800 r/min. **b** Feed force $F_f$ at $n$ = 1800 r/min. **c** Radial force $F_r$ at $n$ = 2800 r/min. **d** Feed force $F_f$ at $n$ = 2800 r/min

flank milling in LTCUVM and CM. As shown in Fig. 10a, b, at the spindle speed $n = 1800$ r/min, both radial force $F_r$ and feed force $F_f$ in LTCUVM were significantly smaller than in CM. A similar trend occurred when the speed was $n = 2800$ r/min as shown in Fig. 10c, d; meanwhile, there was an increasing trend both in the radial force $F_r$ and feed force $F_f$.

#### 4.2.2 Analysis and comparison of surface microstructure

There was an expected response of the surface microstructure to the different cutting edges trajectories in the cases of LTCUVM and CM. In this study, the surface microstructure of two workpieces with different processing conditions was observed by a white light interferometer (Talysurf CCI 6000) and an ultra-depth microscope (KEYENC: VHX-2000C). The test results are shown in Figs. 11, 12, and 13.

Figure 11a, c, and e shows the surface microstructure of the workpiece 3D machined in LTCUVM with rotation speeds $n = 1000$, 2000, and 3000 r/min, respectively. The 3D surface microstructure of the workpieces machined at the same working conditions in CM are shown in Fig. 10b, d, and f. The comparison displayed that the spatial frequency of the contour lines obtained in LTCVUM was higher, but the amplitude was smaller, while the contour lines in CM had the larger range of

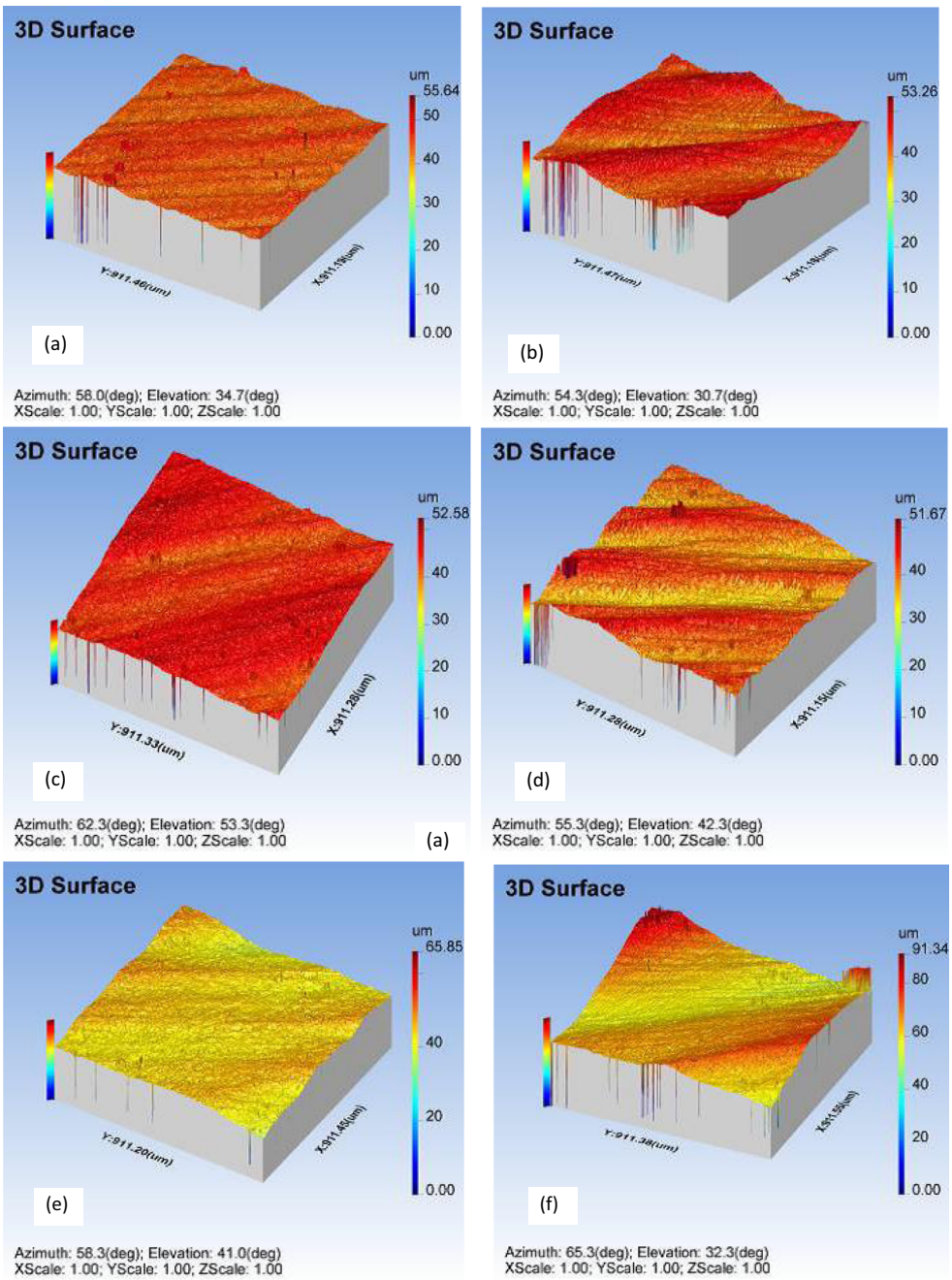


**Fig. 11** 3D Surface morphologies on white light interferometer ($n$ = 1000, 2000, 3000 r/min)

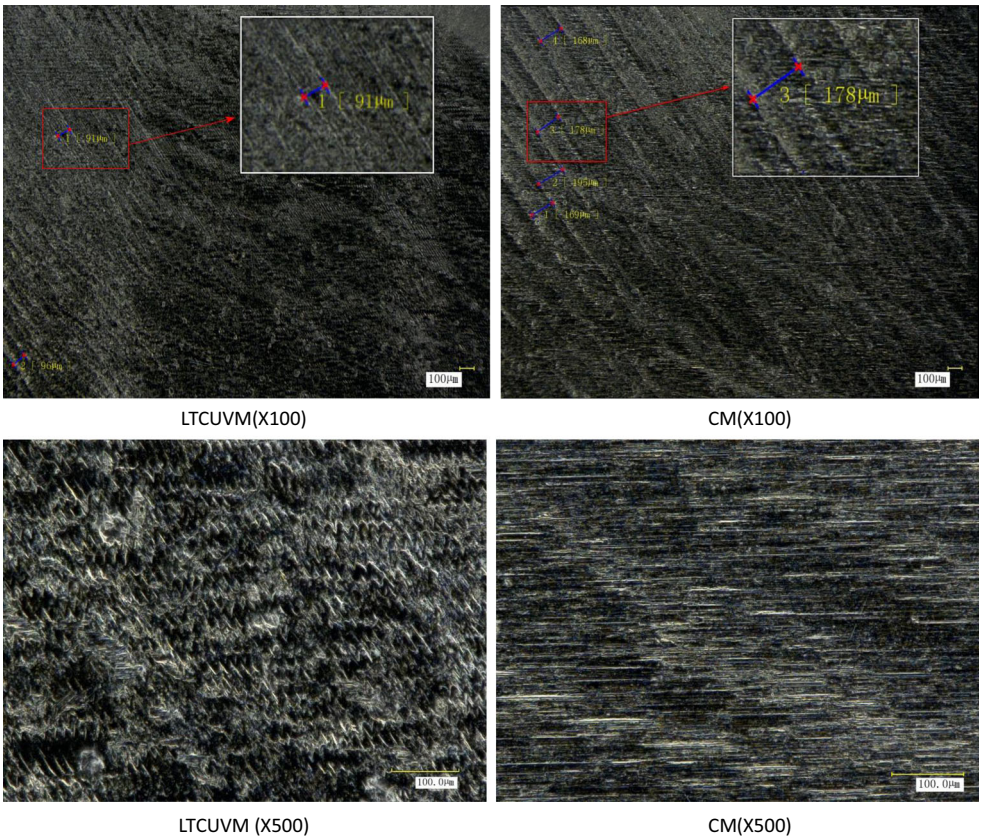


**Fig. 12** Surface microstructure on ultra-depth microscope. **a** LTCUVM (× 100). **b** CM (× 100). **c** LTCUVM (× 500). **d** CM (× 500)

fluctuations, pits, and other defects than in LTCUVM. From the results of the measurements, it can be clearly identified that density and the height of the chatter marks on the surface microstructure of the thin-walled parts in the case of LTVUVM was lower than in CM; moreover, the surface was more flat and smooth from the overall view.

A partial enlarged area of the surface microstructure obtained after two processing methods is shown in Fig. 12. The spindle speed was 1200 r/min. Compared with the × 100-enlargement figure, we can clearly see that fine chatter marks and shallow grooves were obtained in LTCUVM, and the relatively large fluvial spacing in the observation area is 91 μm, while the machined relief is relatively coarse and the grooves are deeper, and the area of the streaking pattern varies from 168 to 195 μm after CM. From the × 500-enlargement view, the surface microstructure after LTCUVM showed a relatively dense fish scale shape, while the surface microstructure obtained by CM is an approximate straight strip shape that followed the cutting tool direction. The relevant literature pointed out that such machined surfaces can improve the oil-locking property of the workpiece surface, improve the quality of machined surfaces, and reduce the tool wear during the machining process [24, 25]; this special microstructure will be investigated in the future to lay the foundation for the development of the field [26].

Three typical machined surface microstructures of a thin-walled workpiece after LTCUVM and CM are shown in Fig. 13 for comparison. The most obvious is an appearance of large deformation and deep chatter marks on the machined surface after CM, which has a negative effect on the finished surface quality. In LTCUVM process, the smaller deformation was obtained with a lower cutting force. Moreover, because of the vibrating separation between the workpiece and tool, the cutting process becomes more delicate, and the tool relieving is weakened; thereby, the shallower chatter marks were obtained. As the spindle speed was increased, there was a trend for the deformation and height of chatter marks increase. The specific analysis and law of change are presented in Section 5 below.

## 5 Experimental results analysis

Several contrast experiments were carried out to estimate the cutter force and surface microstructure of the workpiece being machined in LTCUVM and CM. A number of the cutting force bands were extracted from the experimental cutting force signal to calculate the average value of the cutting force, and the variation trend of the cutting force with the change of the spindle rotation speed in the two machining modes was analyzed. From the results of the white light interference analysis and the super-depth optical microscopy, it could be

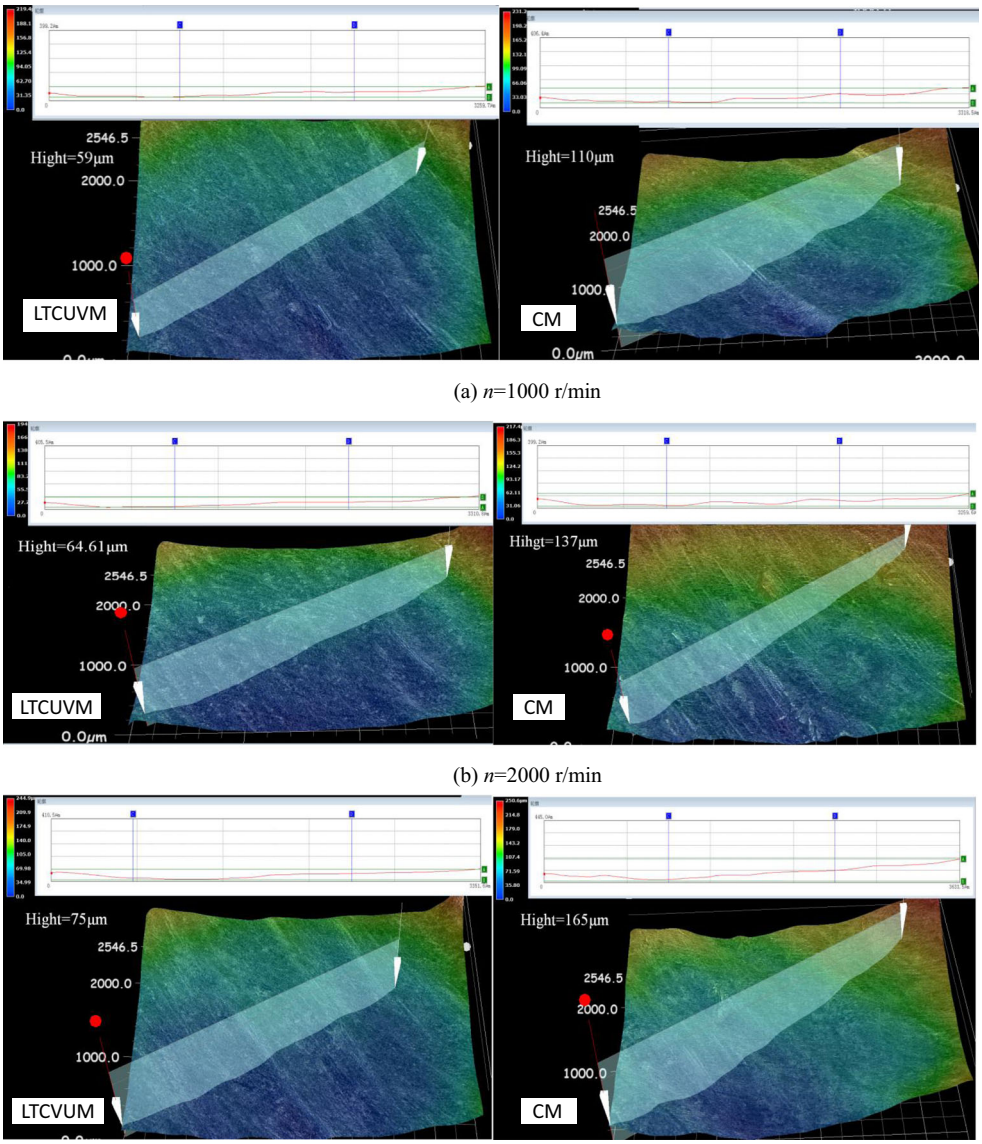


(a) $n$=1000 r/min

(b) $n$=2000 r/min

(c) $n$=3000 r/min

**Fig. 13** 3D depth composite photos of the surface microstructure. **a** $n$ = 1000 r/min. **b** $n$ = 2000 r/min. **c** $n$ = 3000 r/min

preliminarily inferred that the surface microstructure obtained in LTCUVM was superior to the surface microstructure after CM. Then in order to further study the differences in surface microstructure obtained under the two processing methods in a limited area, and explore the changes in surface microstructure with the spindle speed variations, we investigated surface roughness and the height of chatter mark. The experimental dependencies are shown in Figs. 14, 15, and 16.

Figure 14 shows comparison of the spindle speed trends of average cutting forces in the cases of LTCUVM and CM. It can be clearly seen that both radial and feed average cutting forces increase with the speed increase in CM. In the LTCUVM, both cutting forces changed a little with the increase of the rotational speed, and fluctuations took place in a small range at $n$ < 2400 r/min, but after the speed exceeded, the cutting force rose significantly. Further, the reduction ratio increased with the increase of the rotational speed at $n$ < 2400 r/min. Compared with CM, the effect of reducing the cutting force by the vibration processing strengthened, but after $n$ exceeded 2400 r/min, this effect began gradually lessen.

This cutting force change trend is consistent with the change in average cutting force obtained by FEM simulation analysis. This trend also verifies a certain accuracy in the FEM simulation of the cutting force. In general, the FEM cutting force simulation provides forecasts for the experiment, helps exploration of the vibration cutting mechanism, and the analysis of the surface microstructure. Compared to CM, reduction of average cutting forces in LTCUVM undoubtedly changes the state of the workpiece and a tool, the cutter relieving are attenuated, resulting in better surface roughness and microstructure of the machined.

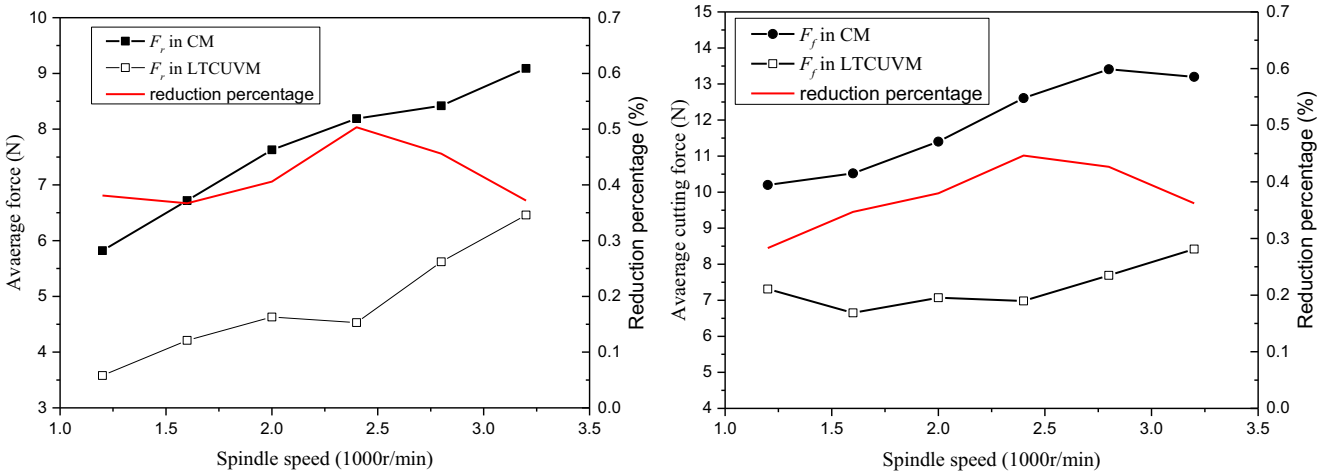


**Fig. 14** Comparison of the cutting forces in LTCUVM and CM vs. spindle speed. **a** Radial force *Fr* vs. spindle speed. **b** Feed force *Ff* vs. spindle speed

The roughness variation is shown in Fig. 15. It can be clearly found that the surface roughness of the titanium alloy thin-walled parts obtained by LTCUVM was significantly less than that obtained by CM. With the speed increase, the surface roughness rose at both processing methods; however, rising was not significant in the case of LTCUVM. The feed rate of the tool rise, with the cutting speed increase also, thus causing the self-excitation of vibrations of the workpiece with increasing amplitude. As a result, more obvious cutter relieving occurred in CM. While, in LTCUVM, high-speed vibration separation cutting can be achieved for workpiece and tool, thus reducing the cutting force. The cutting condition was more delicate at LTCUVM due to special tooltip trajectory, and the overall degree of the cutter relieving was reduced due to the cutting force decrease.

The height of chatter marks on the workpiece surface measured after machining at various speeds is shown in Fig. 16. Obviously, the height of the chatter marks on the surface obtained in the LTCUVM is less than after the CM. With the increase of the rotational speed, there was such a general trend in CM, while until $n = 2400$ r/min there was not an obvious trend in LCTVUM. The results proved that LTCUVM could reduce the height of chatter marks on the workpiece surface.

Comparing with the theoretical part, we found that when $n > 2400$ r/min, the trajectory of the LTCUVM tooltip was no longer displayed a gyration phenomenon. Therefore, it can be inferred that the rotary cutting of the tool in LTCUVM is the main reason for a reduction in the height of surface chatter marks on the surface of the titanium alloy thin-walled part.

As a whole, the basic trends in Figs. 14, 15, and 16 from the experimental results are the following: the cutting force and surface microstructure obtained by LTCUVM is better than by CM. While the increase of spindle speed caused increase in the titanium alloy thin-walled workpiece surface roughness, chatter, and cutter force, however, LTCUVM reduced the impact of the speed increase on the surface microstructure of the machining to some extent, and the gyration cutting of the tool tip may be an important factor in reducing the roughness and height of workpiece chatter marks.

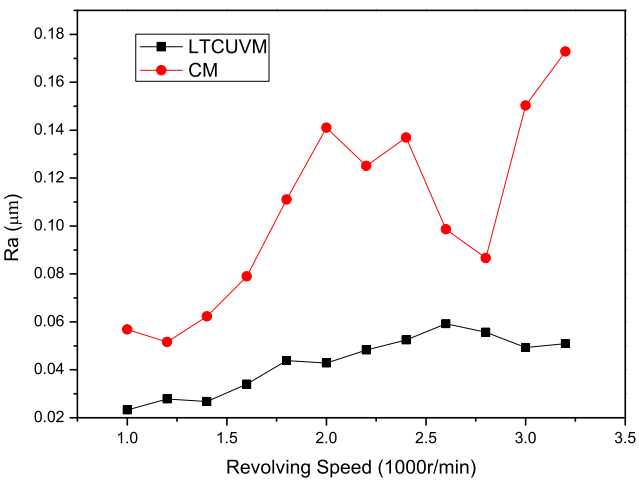


**Fig. 15** Comparison of the surface roughness vs. spindle speed

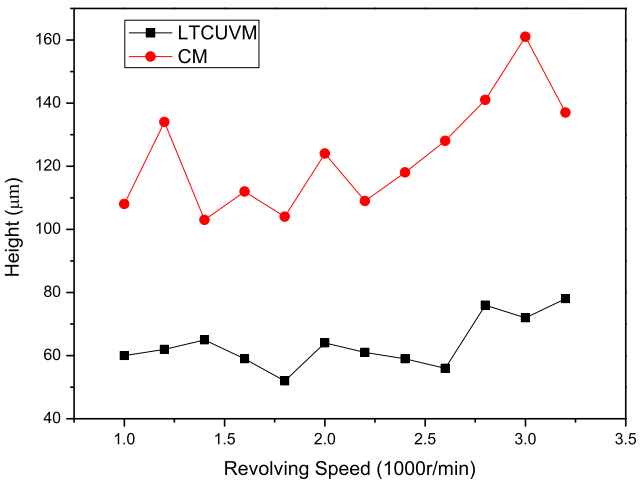


**Fig. 16** Comparison of the chatter marks height on the surface vs. spindle speed

The reduction in the cutting force at LTCUVM provides the cutter relieving reduction that improves the accuracy in the processing of titanium alloy thin-walled parts. As we mentioned above, it was possible to obtain a higher quality surface of the thin-walled workpiece of the titanium alloy by reducing the cutting force on the basis of the gyration and high-frequency cutting in LTCUVM.

## 6 Conclusion

In this paper, we investigated the surface microstructure of the titanium alloy thin-walled parts in flank milling by LTCUVM processing. The theoretical model of the tooltip trajectory of LTCUVM and the duty cycle are proposed, which help to explain the reason why experimental parameters vary with the spindle speed change. Then the cutting simulation FEM was established, and the obtained cutting force signal provided an explanation why the vibration processing reduces the cutting force. Moreover, a specific comparative experiment was designed to verify the accuracy of the FEM. Finally, the machined surface of the titanium alloy thin-walled part was measured and analyzed. According to the analytical model and experiment, the following main research contents and conclusions can be drawn.

1. According to the theoretical model of the tooltip trajectory in the LTCUVM, the duty cycle rises, the rotary and vibration separation cutting as well as the critical speed change with the increase of the spindle speed. Under the parameters set by the simulation, when the spindle speed exceeded 2400 r/min, the rotary cutting of the tool was not generated; when the spindle speed exceeded 3200 r/min, the tool and the workpiece were not separated in LTCUVM.
2. The FEM simulation of the cutting force signal in LTCUVM and CM indicated that the average cutting force at LTCUVM would be reduced by high-frequency vibration separation between the workpiece and tool.
3. The average cutting force variation in the experiment is basically consistent with the results of FEM simulation. The accuracy of the FEM was verified and it provides an exploration of the variation of the cutting force in the vibration cutting mechanism. Therefore, it can be concluded that FEM simulation is an effective and necessary prediction and analysis method for titanium alloy thin-walled parts cutting.
4. The comparison of experimental results obtained by LTCUVM and CM processing showed a less cutting force and smoother machined surface in the case of LTCUVM, and the surface defects were effectively reduced; moreover, the surface of fish scales was observed after LTCUVM. This particular microstructure lays the foundation for the future research.
5. It is possible to weaken the influence of the force deformation of titanium alloy thin-walled parts due to the cutting force reducing, then the cutter relieving reduces by the high-frequency vibration separation cutting in LTCUVM. In turn, better surface roughness and shallower chatter marks were obtained on the surface machined by LTCUVM than by CM.
6. The variation of the cutting force has a good consistency with the roughness and chatter marks height of the machined surface. The cutter force increased and machined surface microstructure of titanium alloy thin-walled parts worsened with an increase of the spindle speed; however, this effect could be reduced by LTCUVM. The rotary cutting of the tooltip is an important factor for the cutter force reducing and for obtaining better surface microstructure in the LTCUVM. The cutting force and machined surface topography changed a little with the change of the spindle speed in the tool rotary cutting regime. When the tool rotary cutting regime finished, the cutting force and machined surface topography changed significantly with the change of the spindle speed in LTCUVM. The advantage of LTVUVM method weakened.

**Funding information** The study received financial support from the Henan Natural Science Foundation (162300410120).



## References

1. Thepsonthi T, Özel T (2015) 3-D finite element process simulation of micro-end milling Ti-6Al-4V titanium alloy: Experimental validations of chip flow and tool wear. J Mater Process Technol 221: 128–145
2. Zhao Xiao Q (2009) Features and special processing method for difficult-to-cut material in aviation industry. Aeronautical Manufacturing Technology 23:50–51
3. Ferry W, Yip-Hoi D (2008) Cutter-workpiece engagement calculations by parallel slicing for five-axis flank milling of jet engine impellers. J Manuf Sci Eng 130(5):383–392
4. Ye HT, Zhang JZ, Yang JF et al (2012) Key application technology of cutting for aircraft difficult-to-machine material. Aeronautical Manufacturing Technology 10:44–46
5. Meshreki M, Attia H, Kö Vecses J (2011) A new analytical formulation for the dynamics of multipocket thin-walled structures considering the fixture constraints. J Manuf Sci Eng 133(2):021014
6. Bolar G, Das A, Joshi SN (2018) Measurement and analysis of cutting force and product surface quality during end-milling of thin-wall components. Measurement 121:190–204
7. Smith S, Dvorak D (1998) Tool path strategies for high speed milling aluminum workpieces with thin webs. Mechatronics 8(4):291–300

8. Sui H, Zhang X, Zhang D, Jiang X, Wu R (2017) Feasibility study of high-speed ultrasonic vibration cutting titanium alloy. J Mater Process Technol 247(19):120–127
9. Harada K, Sasahara H (2009) Effect of dynamic response and displacement/stress amplitude on ultrasonic vibration cutting. J Mater Process Technol 209(9):4490–4495
10. Ma C, Shamoto E, Moriwaki T, Wang L (2004) Study of machining accuracy in ultrasonic elliptical vibration cutting. Int J Mach Tools Manuf 44(12–13):1305–1310
11. Xiao M, Sato K, Karube S, Soutome T (2003) The effect of tool nose radius in ultrasonic vibration cutting of hard metal. Int J Mach Tools Manuf 43(13):1375–1382
12. Nath C, Rahman M (2008) Effect of machining parameters in ultrasonic vibration cutting. Int J Mach Tools Manuf 48(9):965–974
13. Shen XH, Zhang JH, Xing DX, Zhao Y (2012) A study of surface roughness variation in ultrasonic vibration-assisted milling. Int J Adv Manuf Technol 58(5–8):553–561
14. Muhammad R, Ahmed N, Demiral M, Roy A, Silberschmidt VV (2011) Computational study of ultrasonically-assisted turning of Ti alloys. Adv Mater Res 223:30–36
15. Patil S, Joshi S, Tewari A, Joshi SS (2014) Modeling and simulation of effect of ultrasonic vibrations on machining of ti6al4v. Ultrasonics 54(2):694–705
16. Ali Moaz H, Khidhir BA, Ansari MNM, Mohamed B (2013) FEM to predict the effect of feed rate on surface roughness with cutting force during face milling of titanium alloy [J]. HBRC Journal 9.3: 263–269
17. Ducobu F, Arrazola PJ, Rivière-Lorphèvre E, Filippi E (2015) Finite element prediction of the tool wear influence in Ti6Al4V machining. Procedia Cirp 31:124–129
18. Pantalé O, Bacaria J-L, Dalverny O, Rakotomalala R, Caperaa S (2004) 2D and 3D numerical models of metal cutting with damage effects. Comput Methods Appl Mech Eng 193(39–41):4383–4399
19. Molinari A, Musquar C, Sutter G (2002) Adiabatic shear banding in high speed machining of Ti–6Al–4V: experiments and modeling. Int J Plast 18(4):443–459
20. Kay (2002) Failure modeling of titanium6al4v and 2024-t3 aluminum with the Johnson-Cook material model. Technical Rep
21. Zhao W, He N, Li L (2006) Finite element analysis of orthogonal cutting of Ti6Al4V alloy in enhanced cooling condition. J South China Univ Techno: Nat Sci Ed 34(7):40–44
22. Yao YQ, Guo YM, Zhu L et al (2004) Numerical simulation for effect of friction coefficient under high-speed cutting by FEA. J Eng Des 11(1):31–36
23. Meng L (2013) Finite element modelling on high-speed milling process of titantum alloy. Shanghai Jiao Tong University, Shangghai
24. Alavi SH, Cowell C, Harimkar SP (2016) Experimental and finite element analysis of ultrasonic vibrationâ''assisted continuous-wave laser surface drilling. Adv Manuf Process 32(2):216–225
25. Cheng J, Jin Y, Wu J, Wen X, Gong Y, Shi J, Cai G (2016) Experimental study on a novel minimization method of top burr formation in micro-end milling of ti-6al-4v. Int J Adv Manuf Technol 86(5–8):2197–2217
26. Tao G, Zhang J, Shen X, Bai L, Ma C, Wang J (2016) Feasibility study on ultrasonic vibration assisted milling for squamous surface ☆. Proced Cirp 42:847–852